Journal of
Ceramic Science
and Technology

J. Ceram. Sci. Tech., **08** [01] 129-140 (2017)
DOI: 10.4416/JCST2016-00099
available online at: http://www.ceramic-science.com

Structural Studies of Pr Nickelate-Cobaltite – Y-Doped Ceria Nanocomposite

V.A. Sadykov[1, 2], N.F. Eremeev[*1], Z.S. Vinokurov[1, 2], A.N. Shmakov[1, 2, 3], V.V. Kriventsov[1, 3], A.I. Lukashevich[1], A.V. Krasnov[1], A.V. Ishchenko[1, 2]

[1]Boreskov Institute of Catalysis SB RAS, Novosibirsk, 630090, Russia,
[2]Novosibirsk State University, Novosibirsk, 630090, Russia,
[3]Budker Institute of Nuclear Physics SB RAS, Novosibirsk, 630090, Russia.
received October 31, 2016; received in revised form November 2, 2016; accepted January 19, 2017

Abstract

Being stable to carbonization, praseodymium nickelates-cobaltites and their nanocomposites are promising materials for intermediate-temperature solid oxide fuel cells (IT SOFC) cathodes and oxygen separation membranes. This work aims to elucidate specificity of their structure and transport properties on the basis of synchrotron radiation studies. $PrNi_{0.5}Co_{0.5}O_{3-\delta}$ (PNC), $Ce_{0.9}Y_{0.1}O_{2-\delta}$ (YDC), $Ce_{0.65}Pr_{0.25}Y_{0.1}O_{2-\delta}$ (YPDC), CeO_2 and $PrO_{2-\delta}$ powders were synthesized with the Pechini technique. PNC – YDC nanocomposite was obtained via ultrasonic dispersion. The materials were characterized in *in situ* synchrotron XRD analyses with unit cell volume relaxation (CVR) and extended X-ray absorption fine structure (EXAFS). Bulk and surface oxygen mobility and reactivity were studied with O_2 temperature-programmed desorption and CVR methods. Strong cation redistribution between domains was revealed. Fast oxygen diffusion and exchange in the PNC – YDC nanocomposite were shown to be determined by developed interface and variation in the $Pr^{3+/4+}$ cations' charge in the Y-Pr-Ce-O domains. Selected compositions were deposited as functional layers in asymmetric membranes for oxygen separation. According to the test results, the membranes demonstrated promising performance.

Keywords: Oxygen separation membranes, nanocomposites, synchrotron radiation, oxygen mobility, performance

I. Introduction

The design of mixed ionic-electronic conducting (MIEC) oxide and nanocomposite materials is one of the most important tasks in the development of intermediate-temperature solid oxide fuel cells (IT SOFCs) cathodes and oxygen separation membranes [1–3]. State-of-the-art SOFC cathode materials based on Sr-doped perovskites (LSFN, LSFC, LSM, etc.) deteriorate in the intermediate temperature range owing to the segregation of alkaline-earth oxides in the surface layers, the formation of carbonates that block surface sites and chemical interaction at the cathode – electrolyte interface resulting in the formation of La and Sr zirconates that block oxygen transport [4–6]. Sr-free perovskites are apparently more stable to carbonization and more compatible with YSZ with regard to their thermal expansion coefficient [6]. La substitution by smaller cations (e.g. Pr) leads to thermodynamic instability of zirconates $Ln_2Zr_2O_7$, so such materials enable more stable SOFC performance during thermocycling [7]. Developing catalytic membranes reactors for producing syngas from biofuels via selective oxidation by oxygen separated from air including the design of materials for functional layers of such membranes and optimization of their deposition techniques are also important problems. General requirements for the materials are chemical and thermomechanical stability under high gradient of the oxygen chemical potential, high oxygen mobility and surface reactivity, high selectivity in the partial oxidation of fuels into syngas and relatively low cost [8].

Perovskite-like oxides (P) $PrNi_{1-x}Co_xO_{3-\delta}$ and their composites with fluorite-like (F)-doped ceria oxides provide a high overall electric conductivity and very high lattice oxygen mobility and surface reactivity [9–13]. Even in dense nanocomposite ceramics, P and F domains were nanosized and disordered owing to redistribution of the elements between phases. This refers to the transfer of Pr cations into fluorite domains that causes formation of ordered chains of $Pr^{3+/4+}$ cations in the doped ceria matrix (including those at perovskite – fluorite interfaces and domain boundaries), so all oxygen in Pr- and Y-doped ceria is highly mobile[10, 14, 15]. This provides domination of a fast oxygen diffusion channel involving such domains and along P-F interfaces with $D_O \sim 10^{-7}$ $cm^2 \cdot s^{-1}$ at 700 °C, which exceeds values for LSFC and LSFC – GDC by two orders of magnitude [6, 11, 16]. Selected compositions tested as thin film SOFC cathodes demonstrated improved and stable performance as SOFC cathodes in the IT range [9].

In our earlier studies [9–13], $PrNi_{1-x}Co_xO_{3-\delta}$ – YDC nanocomposites sintered into dense ceramics at various temperatures (1000 – 1300 °C) were shown to provide high

* Corresponding author: yeremeev21@gmail.com

oxygen mobility that is comparable to or even better than that of nanocomposites based on LSM, LSFN and LSFC with YSZ, ScCeSZ or GDC electrolytes [6, 17–20]. Disordering of domains of perovskite-like and fluorite phases in Pr-containing systems owing to the redistribution of cations between them was suggested to be responsible for the enhanced oxygen mobility in nanocomposites [10, 21], while for LSM-, LSFN- and LSFC-based cathode nanocomposites with electrolytes the non-additive increase of oxygen mobility was assigned only to the effect of the well-developed perovskite-fluorite interface [6, 17–20]. The best performance for PNC and PNC – YDC sintered at 1000 and 1100 °C was shown [10, 11].

However, structural features of PNC and PNC – YDC systems and their correlation with the performance of these materials at conditions close to those in operation have still not been studied thoroughly. This paper aims to elucidate the structural specificity of the Pr-nickelates (nickelates-cobaltites)-based materials. Their real structure/microstructure, bulk oxygen mobility and surface reactivity were studied by applying a combination of structural methods (*in situ* synchrotron XRD, TEM, EXAFS) and several techniques for characterization of their transport properties (temperature-programmed desorption of oxygen (TPD O_2), unit cell volume relaxation (CVR)). Selected materials with the most promising characteristics were tested as thin asymmetric membranes for oxygen separation.

II. Experimental

Nanocrystalline oxides $Pr_{1-z}Ni_{1-x}Co_xO_{3-\delta}$ ($PN_{1-x}C$; $x = 0 \div 0.6$; $z = 0, 0.2$), $Ce_{0.9}Y_{0.1}O_{2-\delta}$ (YDC), $Ce_{0.65}Pr_{0.25}Y_{0.1}O_{2-\delta}$ (YPDC), CeO_2 and $PrO_{2-\delta}$ were synthesized with the modified polymerized complex precursor (Pechini) technique [6] using water solutions of metal nitrates. PNC – YDC nanocomposite was obtained via ultrasonic dispersion of individual powders in propane-2-ol in the weight ratio 1:1 using a T25 (ULTRA-TURRAX IKA, Germany) homogenizer. Optimal sintering temperatures were chosen to show better performance according to our earlier studies [10, 11]. The PNC samples were calcined at 1000 °C, the other ones at 1100 °C.

To determine the phase composition, unit cell parameters and domain sizes of the samples, X-ray diffraction (XRD) was applied using a D8 Advance (Bruker, Germany) using CuK_α monochromatic radiation ($\lambda = 1.5418$ Å) in 2θ range 5 – 90 °. The cell parameters were refined with PCW software (version 2/4), with the average uncertainty of estimation ~ 0.002 Å.

Time-resolved *in situ* SXRD experiments were carried out at the SSTRC "Precise diffraction-2" station equipped with the position-sensitive detector OD-3M-350 [13, 22], the residual gas analyzer (RGA, QMS 100 series, Stanford research systems) and the high-temperature XRD reactor chamber XRK-900 (Anton Paar GmbH, Austria). The working wavelength of 0.1021 nm was set by a single reflection from a perfect flat crystal of Si(220). The analysis of SXRD patterns was performed with MAUD software [23].

To elucidate the real/defect structure and microstructure of nanocomposites (sizes and local chemical compositions of domains, their shapes and disordering, characteristics of domain boundaries and extended defects) high-resolution transmission electron microscopy (TEM) was applied using a JEM-2010 instrument (Jeol, Japan) (lattice resolution 1.4 Å, acceleration voltage 200 kV). The local elemental composition was analyzed with an energy-dispersive EDX spectrometer equipped with Si(Li) detector (energy resolution 130 eV).

The EXAFS spectra (Ce-L_3 and Pr-L_3 edges) were obtained at the "EXAFS spectroscopy" station at the SSTRC using Si(111) crystal monochromator. *In situ* extended X-ray absorption fine structure spectroscopy (EXAFS) studies of Ce-L_3 and Pr-L_3 edges were performed at the "EXAFS spectroscopy" station using Si(111) crystal monochromator with an energy resolution of 6000 and harmonic neutralization. Both X-ray absorption fine structure (XAFS) and X-ray absorption near-edge (XANES) spectra were analyzed [13, 24]. The EXAFS spectra obtained were treated using Viper software [25, 26]. The initial point of the spectrum ($k = 0$) was the inflection point of the edge. Coordination distances R and coordination numbers were obtained by fitting with DL_Excurv 6 software according to the XRD data. The relative errors estimated for coordination numbers and distances are 10 % and 1 % respectively.

The temperature-programmed desorption of oxygen (O_2 TPD) in a He stream was used to characterize the bonding strength of oxygen with the surface of the perovskites and nanocomposites and the amount of easily desorbed/mobile oxygen [6, 18, 20, 21]. It was studied in a micro-catalytic flow reactor system after pretreatment of samples in O_2 at 500 °C for 2 h using the temperature ramp 5 °C min^{-1} from 25 to 880 °C followed by the isotherm for 60 min at 880 °C. The oxygen content in the exit stream was determined with a TEST-1 (Boner, Russia) gas analyzer. To estimate the activation energy of desorption as a measure of the oxygen bonding strength, desorption rate curves were fitted with Gauss components. The effective activation energy was estimated by analyzing the ascending part of the peak profile using the Wigner-Polanyi equation [27].

Since cathode layers in fuel cells operate under the gradient of the oxygen chemical potential, estimation of their surface reactivity and transport properties in these conditions is required as well [4, 5]. For dense pellets, the chemical diffusion coefficients D_{chem} and surface exchange constant k_{chem} were estimated based on analysis of their unit cell volume relaxation after step-wise change of the O_2 content in the gas flow [20, 28]. By assuming a linear reaction rate on the surface and the approximation of infinite plate model, the analytical solution for normalized unit cell volume relaxation (CVR) curves [6, 18, 20, 28] can be described by Eq. 1:

$$\frac{V - V_0}{V_\infty - V_0} = 1 - \sum_{n=0}^{\infty} \frac{2L^2}{\beta_n^2\left(\beta_n^2 + L^2 + L\right)} \cdot \exp\left(-\beta_n^2 D_{chem} t / l^2\right), \quad (1)$$

where V is the unit cell volume; t is time; "0" and "∞" subscripts correspond to the initial and final equilibrium state of the samples; L is described by Eq. 2:

$$L = \frac{lk_{chem}}{D_{chem}}, \quad (2)$$

l is effective XRD penetration depth [28]; and β_n coefficients are n-ths roots of the transcendental Eq. 3:

$$\beta_n \cdot \tan(\beta_n) = L. \quad (3)$$

To prepare asymmetric membranes for oxygen separation, a few PNC – YDC functional layers (mesoporous, microporous and dense), dense $MnFe_2O_4$ – $Ce_{0.9}Gd_{0.1}O_{2-\delta}$ buffer layer and porous Pt (1.4 wt. %)/ $Sm_{0.15}Pr_{0.15}Ce_{0.35}Zr_{0.3}O_{2-\delta}$ catalytic layer were consecutively deposited on a Ni/Al foam substrate. Each layer was sintered at 1100 °C (900 °C for catalytic layer).

The membranes obtained were tested in CH_4 selective oxidation into syngas/oxidry reforming using a specially built setup, oven-placed double-flange assembly.

III. Results and Discussion

(1) Structural and microstructural characterization of nanocomposite materials

(a) *X-ray diffraction*

According to our previous studies [9–13], for $PrNi_{1-x}Co_xO_{3-\delta}$ ($x = 0.4 \div 0.6$) samples calcined at temperatures up to 1100 °C, the crystal structure corresponds to orthorhombic perovskite phase [29] with some admixture of $PrO_{2-\delta}$ phase. After sintering at temperatures higher than 1100 °C, the $PrO_{2-\delta}$ oxide disappears while admixture of $Pr_4(Ni,Co)_3O_{10+\delta}$ phase emerges. According to *in situ* SXRD data, PNC was a stable orthorhombic perovskite (P) during heating in air up to 850 °C (Fig. 1). Fluorite-like $PrO_{2-\delta}$ admixture (amount ~ 8 wt. %) was shown to change the symmetry from monoclinic to cubic during heating, and after cooling back to monoclinic again. For $PrNi_{1-x}Co_xO_{3-\delta}$ – YDC (1:1) composites sintered at temperatures up to 1100 °C the structure of both perovskite and fluorite phases is preserved, although pronounced redistribution of cations between domains of P and F phases takes place. The most prominent feature is the incorporation of Pr cations into the doped ceria phase, most likely disordering both perovskite-like and fluorite-like phases [10, 11]. Strong Pr cation redistribution was shown to take place between P and F phases, the average compositions of which were $Pr_{0.8}Ni_{0.5}Co_{0.5}O_{3-\delta}$ and $Ce_{0.65}Pr_{0.25}Y_{0.1}O_{2-\delta}$ according to TEM with EDX analysis data [11]. At higher (1300 °C) sintering temperature, redistribution of elements in nanocomposites results in transformation of the perovskite structure into the cubic one [9, 10]. Cell parameters of the materials studied are given in the Tables 1 and 2. To elucidate structure evolution in PNC and PNC – YDC, *in situ* SXRD studies were carried out for separately synthesized oxide phases as well. $PrO_{2-\delta}$ ($nPrO_2 \cdot Pr_2O_3$) oxide changes its structure during heating in air from $Pr_{12}O_{22}$ (s.g. P21/c) to Pr_6O_{11} (s.g. Fm(-)3m) and Pr_7O_{12} (s.g. R(-)3) (Fig. 2). The $Ce_{0.65}Pr_{0.25}Y_{0.1}O_{2-\delta}$ sample actively loses oxygen during heating in He. More details can be found in our previous study [13].

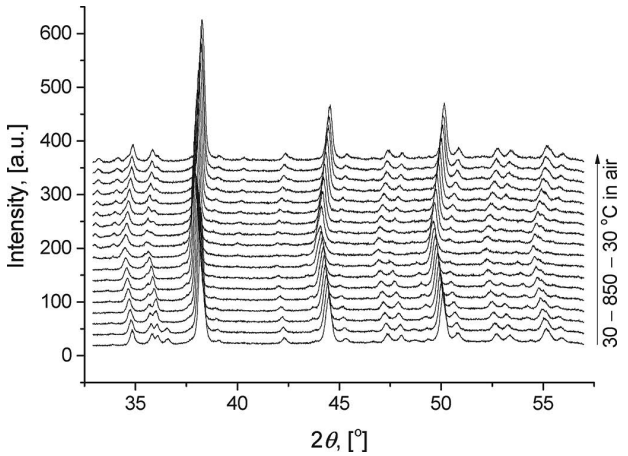

Fig. 1: *In situ* SXRD patterns of $PrNi_{0.5}Co_{0.5}O_{3-\delta}$ sample sintered at 1000 °C.

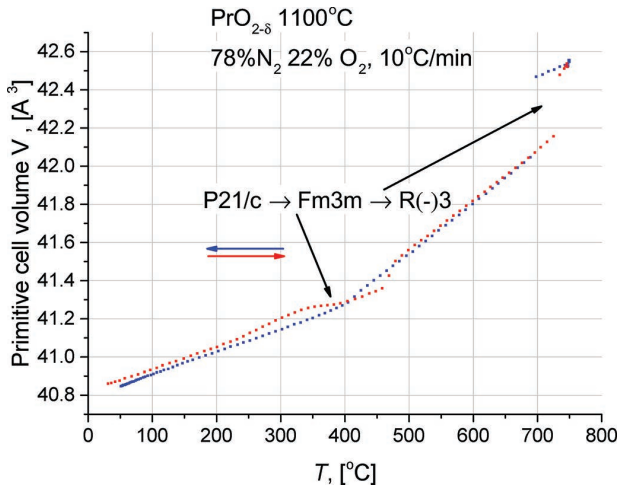

Fig. 2: Variation of $PrO_{2-\delta}$ structure during heating and cooling in air.

(b) *Transmission electron microscopy*

TEM with EDX analysis data agrees with XRD [11] and SXRD [13] data. Various types of extended defects present in domains of both phases are shown in Fig. 3. For the $PrNi_{0.5}Co_{0.5}O_{3-\delta}$ – YDC composite sintered at 1100 °C, the average P phase composition is about $Pr_{0.8}Ni_{0.5}Co_{0.5}O_{3-\delta}$, while the F phase composition is about $Ce_{0.65}Y_{0.1}Pr_{0.25}O_{2-\delta}$. In addition, Ni and Co cations were transferred into the fluorite domains, mainly into their surface layers [6, 10, 18], while an amount of Y was found in the perovskite domains (Fig. 3). Statistical analysis of EDX data for different domains revealed that domains of the same phase differ strongly with regard to their elemental composition, so in some F domains Pr cations were not detected at all. This demonstrates that the chemical composition of the domains is controlled by kinetic factors and not by equilibrium. However, on average, there are some apparent trends in variation of the averaged lattice parameters in both phases with the sintering temperature and composition of perovskite phase (Table 2). For fluorite phase, the lattice parameter decreases with the sintering temperature, which can be explained by increasing the content of Pr^{4+} cations ($r = 0.95$ Å [30]) and decreasing the content of Y cations ($r = 1.014$ Å [30]).

Indeed, in Pr-doped ceria the lattice parameter was found to increase with the Pr content when samples were slowly cooled in air after sintering [31, 32]. For the perovskite phase in the nanocomposites, the unit cell volume also decreases with the sintering temperature (Table 2), while it increases for separate P phases (Table 1). In agreement with the trend observed for fluorite phase in nanocomposite as well as EDX data (vide supra), this implies that the content of Pr^{3+} cations in PNC domains responsible for expansion of perovskite lattice decreases with the sintering temperature. Domain sizes of both phases in samples sintered at 1100 °C are in the range of 50 – 100 nm, thus providing a developed interface.

Table 1: Unit cell parameters of $PrNi_{1-x}Co_xO_{3-\delta}$ perovskites.

T_{sint}, °C	Unit cell parameters			
Ni/Co ratio	*a*, Å	*b*, Å	*c*, Å	*V*, Å^3
900				
04/06	5.376	7.613	5.403	221.16
05/05	5.409	7.619	5.381	221.75
06/04	5.380	7.620	5.410	221.75
1000				
04/06	5.378	7.615	5.405	221.37
05/05	5.415	7.626	5.385	222.40
06/04	5.385	7.626	5.418	222.52

Table 2: Unit cell parameters of $PrNi_{1-x}Co_xO_3$ perovskites and fluorite in nanocomposites.

T_{sint}, °C	Perovskite				Fluorite
Ni/Co ratio	*a*, Å	*b*, Å	*c*, Å	*V*, Å^3	*a*, Å
900					
04/06	5.377	7.614	5.401	221.12	5.409
05/05	5.382	7.619	5.406	221.68	5.410
06/04	5.383	7.625	5.410	222.05	5.411
1000					
04/06	5.373	7.608	5.396	220.58	5.406
05/05	5.380	7.613	5.401	221.21	5.407
06/04	5.385	7.619	5.407	221.84	5.408
1100					
04/06	5.371	7.601	5.393	220.17	5.402
05/05	5.375	7.604	5.396	220.54	5.403
06/04	5.385	7.613	5.400	221.38	5.406

Apparently good ordering of lattice fringes in the high-resolution TEM image of $Ce_{0.65}Y_{0.1}Pr_{0.25}O_{2-\delta}$ sample particles (Fig. 4a) was observed, which agrees with narrow diffraction peaks in the sample and demonstrates its good crystallinity. However, variation of the image contrast might suggest some non-uniformity of the spatial distribution of dopants. Meanwhile, for the $Pr_{0.8}Ni_{0.5}Co_{0.5}O_{3-\delta}$ sample sintered at 1100 °C, the high-resolution TEM image (Fig. 4b) revealed the presence of extended defects (stacking faults, domain boundaries and microinclusions) indicated by arrows.

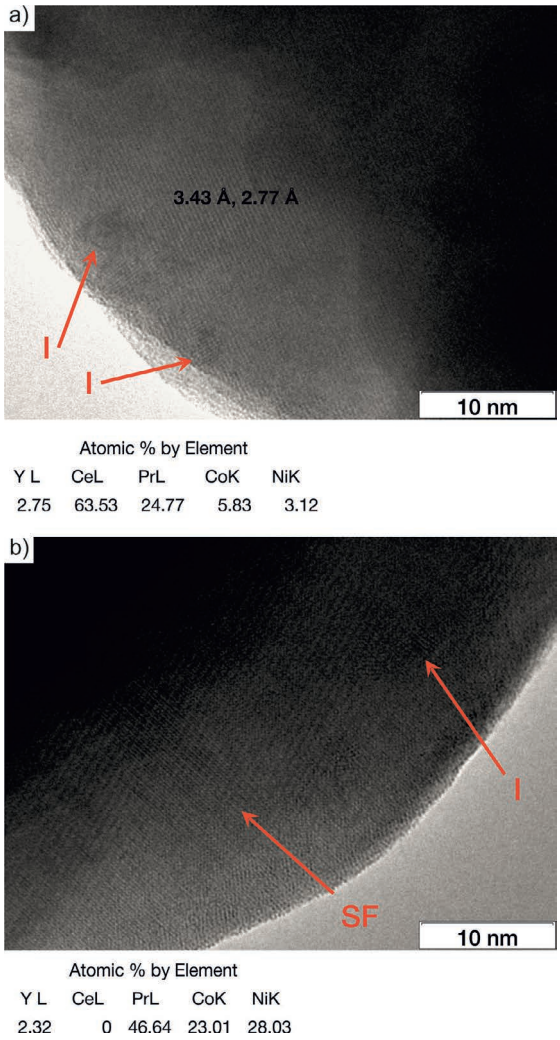

Fig. 3: High-resolution images of neighboring domains of fluorite (a) and perovskite (b) phases in nanocomposite $PrNi_{0.6}Co_{0.4}O_{3-\delta}$ – $Ce_{0.9}Y_{0.1}O_{2-\delta}$ sintered at 1000 °C with corresponding EDX spectra and elemental composition. I – inclusions, SF – stacking faults.

(c) *EXAFS*

EXAFS analysis was used to study the local structure around Pr and Ce atoms and elucidate the effect of cation redistribution on the distortion of P and F structures and the formation of oxygen vacancies, since Pr cations are known to change their charge easily [33]. $PrNi_{0.5}Co_{0.5}O_{3-\delta}$ and $PrNi_{0.5}Co_{0.5}O_{3-\delta}$ (50 wt%) – $Ce_{0.9}Y_{0.1}O_{2-\delta}$ samples were studied in comparison with the $PrO_{2-\delta}$, CeO_2, $Ce_{0.9}Y_{0.1}O_{2-\delta}$, $Ce_{0.65}Pr_{0.25}Y_{0.1}O_{2-\delta}$ and $Pr_{0.8}Ni_{0.5}Co_{0.5}O_{3-\delta}$ samples and reagent grade

$Pr(NO_3)_3 \cdot 6H_2O$ and $Ce(NO_3)_3 \cdot 6H_2O$ ones. As follows from EXAFS analysis data, Ce cations are generally charged 4+ for PNC – YDC, while Pr ones are 3+ in general for PNC and both 3+ and 4+ for PNC – YDC nanocomposite. This is in agreement with the data on oxygen mobility and surface reactivity studies carried out previously [11]. Pr and Ce coordination numbers obtained from radial distribution functions are revealed to be close to those in slightly distorted orthorhombic P and cubic F structures. Ce-L_3 edge spectra for nanocomposite is similar to YPDC with the difference explained by local Pr:Ce ratio variation and structure distortion. Thus, generally Pr^{3+} migration from P to F phase and its charge variation may cause the formation of additional vacancies. This agrees with data obtained in the current and previous works [11]. As we reported earlier [13], the intensity of the EXAFS peaks corresponding to the Ce-O and Ce-Me coordination shell declines with increasing dopant content. The lower Ce-O peak corresponds to a higher oxygen vacancies concentration in Ce coordination sphere. The normalized XANES spectra on the Pr-L_3 edge for series of the samples are given in Fig. 5.

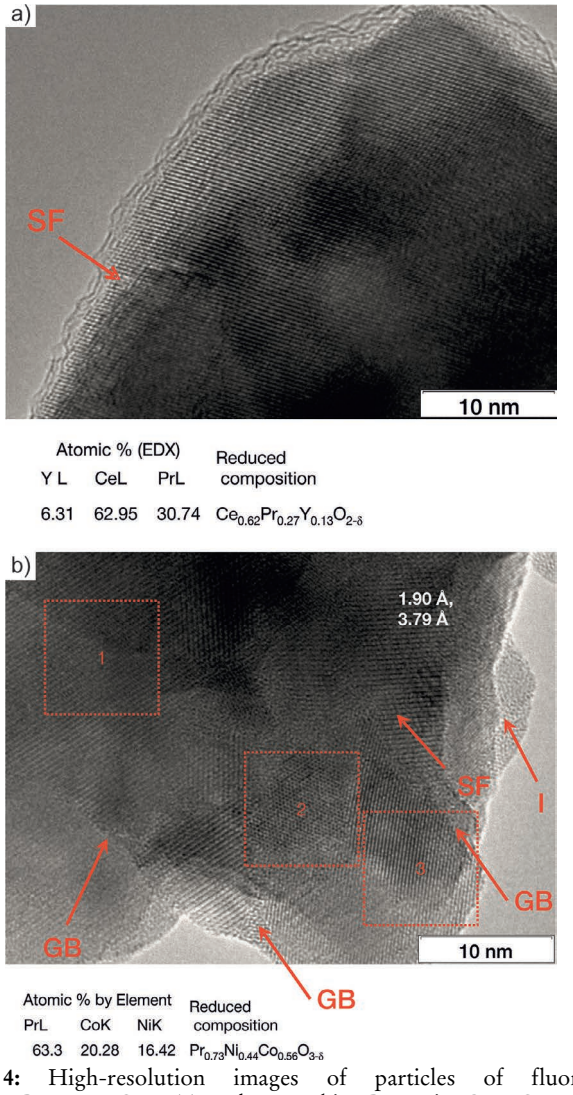

Fig. 4: High-resolution images of particles of fluorite $Ce_{0.65}Pr_{0.25}Y_{0.1}O_{2-\delta}$ (a) and perovskite $Pr_{0.8}Ni_{0.5}Co_{0.5}O_{3-\delta}$ (b) samples sintered at 1100 °C with corresponding EDX spectra and elemental composition. I – inclusions, SF – stacking faults, GB – grain boundaries.

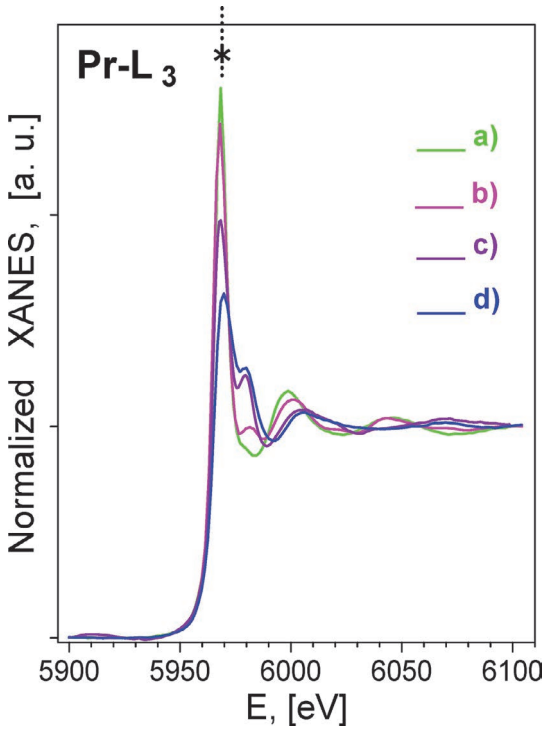

Fig. 5: Normalized XANES spectra (Pr-L_3 edge) of $Pr(NO_3)_3$ (a) and $PrNi_{0.5}Co_{0.5}O_{3-\delta}$ (b), PNC-YDC (c) and Pr_6O_{11} (d) samples sintered at 1100 °C. Reprinted from Sadykov *et al.* Physics Procedia (2016, in press).

(2) Mobility and reactivity of oxygen

(a) *Temperature-programmed oxygen desorption*

As follows from Fig. 6, PNC perovskites calcined at 1000 °C demonstrate intense oxygen desorption in several (3 or 4) peaks situated in the intermediate temperature range and one high-temperature peak at 880 °C, which is similar to Pr nickelates with Ruddlesden – Popper structure [21]. However, peaks situated in the intermediate temperature range are less intense than the high-temperature one, and the total amount of desorbed oxygen is less than in the case of Pr nickelates [21] (Table 3). Nonetheless, the amount of oxygen desorbed in each peak is sufficiently high, which implies oxygen removal from the bulk of particles. A low activation energy of desorption suggests low activation barriers for the oxygen migration as well (Table 3). In the case of perovskites, these low-temperature peaks can be assigned to the presence of some extended defects (stacking faults, domain boundaries, etc.) [6] with the local coordination environment of Pr cations similar to that in R-P type structure. Indeed, the total amount of oxygen desorbed in TPD run is not higher than 10 – 15 monolayers (~ 1 % of the total amount of oxygen in samples, Table 3), thus corresponding to some defects. This assignment agrees with strong variation or even suppression of oxygen desorption in the intermediate temperature range after sintering of the perovskites at a higher (≥ 1100 °C) temperature (Fig. 7), which can result in annealing of some defects as well as decreasing Pr^{4+} content. For the perovskite samples sintered at 1000 – 1100 °C, the effective activation energy of desorption ($E_{a,\,TPD}$) tends to increase with the peak T_{max}, which can be explained by the

increase of the bonding strength of surface oxygen forms removed in the rate-limiting stage (heat of Me-O adsorption varying in the range of 50 – 400 kJ·mol^{-1} [6]). A lower $E_{a,\,TPD}$ for high-temperature peaks in the perovskites and the intermediate-temperature peak in nanocomposites (Table 3) can be explained by the change of the rate-limiting stage of desorption from the surface-controlled to the bulk-controlled one via the cooperative mechanism of oxygen migration in the coordination sphere of Pr cations with the activation barrier as low as 20 – 30 kJ·mol^{-1} [21].

Table 3: Amount of oxygen desorbed q_{O_2} and effective activation energy of oxygen desorption $E_{a,\,TPD}$ for samples sintered at 1000 °C and 1100 °C.

Peak No.	T_{max}, [°C]	q_{O_2}, [monolayers]	q_{O_2}, [% of total desorbed]	$E_{a,\,TPD}$, [kJ/mol]
		$PrNi_{0.4}Co_{0.6}O_{3-\delta}$, 1000 °C		
1	390	0.8	8	130
2	470	0.6	6	290
3	550	1.6	15	360
4	880*	7.3	71	200
	Total desorbed	10	100 (1 % of total oxygen)	
		$PrNi_{0.5}Co_{0.5}O_{3-\delta}$, 1000 °C		
1	390	0.6	6	50
2	470	0.3	3	140
3	550	0.7	7	190
4	880*	7.9	84	150
	Total desorbed	9	100 (1 % of overall oxygen)	
		$PrNi_{0.6}Co_{0.4}O_{3-\delta}$, 1000 °C		
1	300	0.3	2	190
2	390	0.3	2	140
3	500	0.2	1	300
4	590	0.6	4	340
5	880*	14	93	120
	Total desorbed	15	100 (1 % of overall oxygen)	
		$PrNi_{0.4}Co_{0.6}O_{3-\delta}$ – YDC, 1100 °C		
1	480	7.7	52	70
2	880*	7.2	48	50
	Total desorbed	15	100 (1 % of overall oxygen)	
		$PrNi_{0.5}Co_{0.5}O_{3-\delta}$ – YDC, 1100 °C		
1	460	9	53	60
2	880*	8	47	50
	Total desorbed	17	100 (1 % of overall oxygen)	
		$PrNi_{0.6}Co_{0.4}O_{3-\delta}$ – YDC, 1000 °C		
1	440	6.5	43	60
2	880*	8.5	57	70
	Total desorbed	15	100 (1 % of overall oxygen)	

Peak No.	T_{max}, [°C]	q_{O_2}, [monolayers]	q_{O_2}, [% of total desorbed]	$E_{a,\ TPD}$, [kJ/mol]
$PrNi_{0.4}Co_{0.6}O_{3-\delta}$, 1100 °C				
1	450	3.3	17	80
2	570	2	10	270
3	880*	14	73	240
	Total desorbed	19	100 (1 % of overall oxygen)	
$PrNi_{0.5}Co_{0.5}O_{3-\delta}$, 1100 °C				
1	880*	20	100	150
	Total desorbed	19	100 (1 % of overall oxygen)	
$PrNi_{0.4}Co_{0.6}O_{3-\delta}$ – YDC, 1100 °C				
1	490	25	49	90
2	880*	27	51	9
	Total desorbed	52	100 (2 % of overall oxygen)	
$PrNi_{0.5}Co_{0.5}O_{3-\delta}$ – YDC, 1100 °C				
1	470	24	57	110
2	880*	23	43	25
	Total desorbed	47	100 (3 % of overall oxygen)	
$PrNi_{0.6}Co_{0.4}O_{3-\delta}$ – YDC, 1100 °C				
1	460	20	51	90
2	880*	19	49	25
	Total desorbed	39	100 (3 % of overall oxygen)	

* Peak maximum at isothermal conditions (T = 800 °C, t = 70 min).

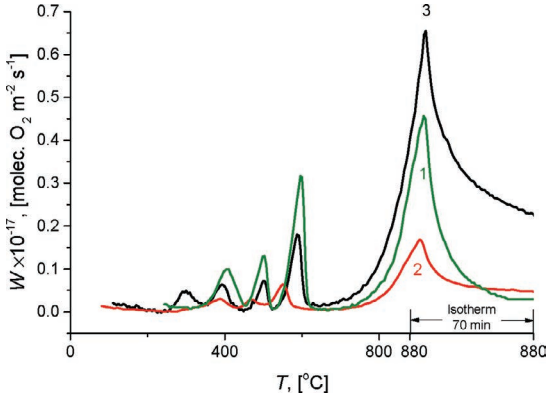

Fig. 6: O_2 TPD spectra for perovskite samples sintered at 1000 °C. 1 – $PrNi_{0.4}Co_{0.6}O_{3-\delta}$, 2 – $PrNi_{0.5}Co_{0.5}O_{3-\delta}$, 3 – $PrNi_{0.6}Co_{0.4}O_{3-\delta}$.

In PNC – YDC composites much more intense desorption in the intermediate-temperature range is observed (Fig. 8), while the total amount of oxygen desorbed in the run increases up to 20 monolayers (Table 3). For composites, the increase in the sintering temperature from 1000 to 1100 °C even enhanced the desorption peak at ~ 460 °C while decreasing the intensity of the high-temperature peak (Figs. 8, 9) and increasing the total amount of oxygen desorbed in TPD run up to 40 – 50 monolayers (Table 3). This trend is retained even for PNC – YDC nanocomposites sintered at 1300 °C [9], for which the maximum rate of O_2 desorption in the peak at ~ 450 °C is increased up to $4 \cdot 10^{17}$ molecules $O_2 \cdot m^{-2} \cdot s^{-1}$. The most unique feature of O_2 desorption patterns for PNC – YDC nanocomposites is domination of the intermediate-temperature desorption peak, which is not observed for other perovskite-fluorite nanocomposites (LSFN(C) – GDC, LSM – GDC, etc. [6]). Note that for ceria doped with Ln^{3+} (La, Sm) cations, the oxygen desorption is also observed mainly in the high-temperature range with the total amount of oxygen desorbed in the run in the range of 0.2 monolayers [34]. Hence, namely Pr incorporation into the doped ceria domains appears to be responsible for such fast oxygen diffusion in PNC – YDC nanocomposites. Indeed, according to Sinev *et al.* [15], for $Pr_{0.55}Ce_{0.45}O_{2-\delta}$ fluorite fast release of the lattice oxygen occurs in the same middle-temperature range of 400 – 500 °C. This is provided by easy variation of the charge state of Pr cations in mixed oxides while changing the oxygen partial pressure as revealed by XPS [14, 15] and *in situ* optical absorption [35] studies. Ordered chains of $Pr^{3+/4+}$ cations in the doped ceria matrix (including those at interfaces and domain boundaries) are thought to ensure fast charge transfer and rapid oxygen diffusion [14, 15, 35]. On the other hand, disordering of perovskite-like structures due to cation migration in nanocomposites along with generation of anion vacancies and decreasing the average strength of Me-oxygen bond owing to the presence of Ni cations [29, 36, 37] could also help to increase the oxygen mobility in perovskite-like domains by decreasing the energy barrier of oxygen atoms jumps through triangles comprising one A atom and two B atoms [6, 38]. Balance of effects caused by all these factors seems to be responsible

for providing the highest oxygen mobility for the composite with the highest amount of Ni in the series of samples sintered at 1000 °C (Fig. 8), while after sintering at 1100 °C it demonstrates the lowest peak rate, although the difference between the samples is small in this case (Fig. 9).

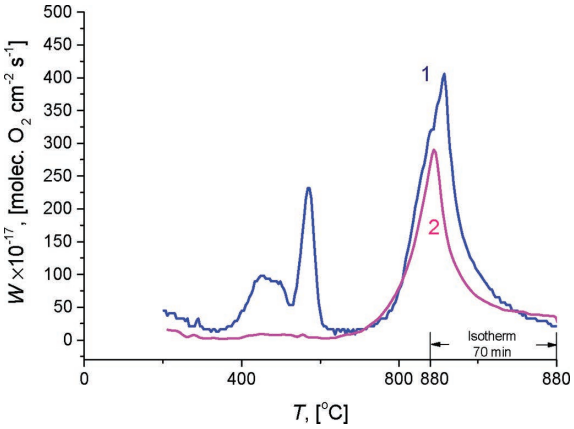

Fig. 7: O_2 TPD spectra for perovskite samples sintered at 1100 °C. 1 – $PrNi_{0.4}Co_{0.6}O_{3-\delta}$, 2 – $PrNi_{0.5}Co_{0.5}O_{3-\delta}$.

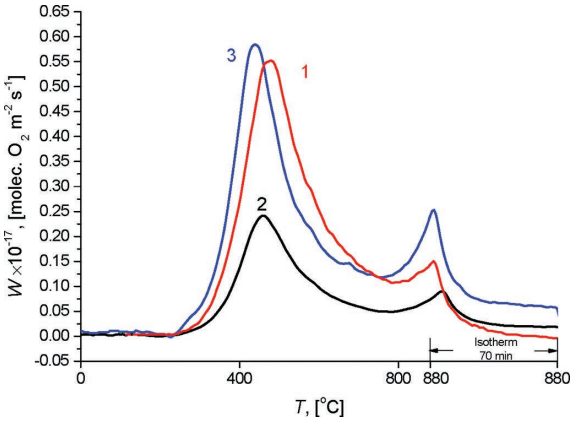

Fig. 8: O_2 TPD spectra for nanocomposite samples sintered at 1000 °C. 1 – $PrNi_{0.4}Co_{0.6}O_{3-\delta}$ – YDC, 2 – $PrNi_{0.5}Co_{0.5}O_{3-\delta}$ – YDC, 3 – $PrNi_{0.6}Co_{0.4}O_{3-\delta}$ – YDC.

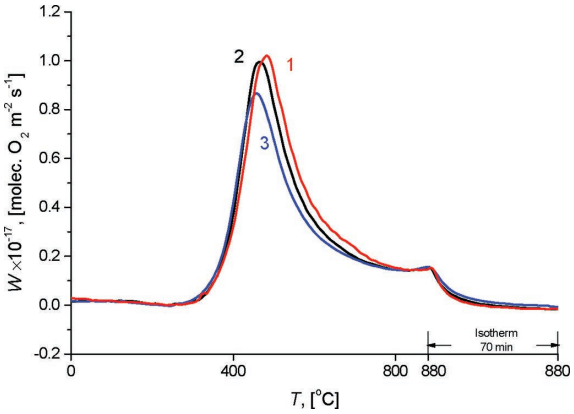

Fig. 9: O_2 TPD spectra for nanocomposite samples sintered at 1100 °C. 1 – $PrNi_{0.4}Co_{0.6}O_{3-\delta}$ – YDC, 2 – $PrNi_{0.5}Co_{0.5}O_{3-\delta}$ – YDC, 3 – $PrNi_{0.6}Co_{0.4}O_{3-\delta}$ – YDC.

(b) *Oxygen chemical diffusion coefficients*

The oxygen mobility and surface reactivity in the presence of chemical potential gradient were studied also for all samples based on analysis of the cell volume relaxation (CVR) curves obtained from the SXRD data after abrupt change of the oxygen partial pressure. Typical CVR plots are given in Fig. 10. For PNC – YDC, $k_{chem} = 1.2 \cdot 10^{-7}$ cm·s^{-1} at 600 °C (Fig. 11a), D_{chem} cannot be estimated accurately owing to the process being limited by the surface exchange. Arrhenius plot of D_{chem} and k_{chem} for PNC – YDC compared to YPDC and $PrO_{2-\delta}$ are given in Fig. 11 with the details being provided in our previous study [13].

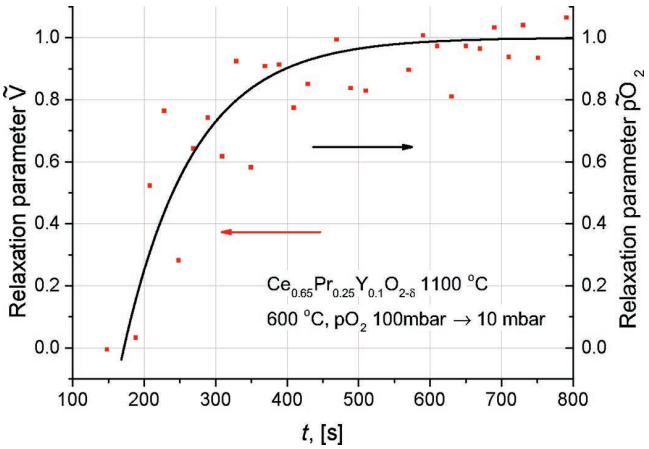

Fig. 10: Fluorite phase unit cell volume relaxation plot for the $PrNi_{0.5}Co_{0.5}O_{3-\delta}$ – $Ce_{0.9}Y_{0.1}O_{2-\delta}$ sample sintered at 1100 °C.

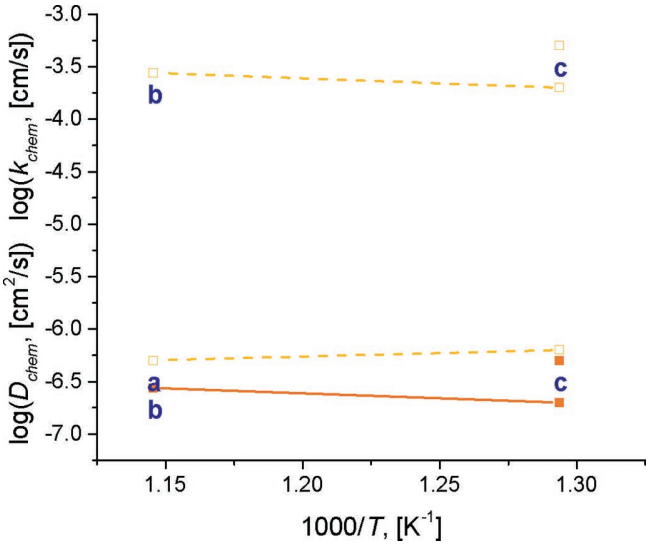

Fig. 11: Arrhenius plots for chemical diffusion coefficients (D_{chem}) and chemical exchange constant (k_{chem}) for $PrNi_{0.5}Co_{0.5}O_{3-\delta}$ – $Ce_{0.9}Y_{0.1}O_{2-\delta}$ (a), $Ce_{0.65}Pr_{0.25}Y_{0.1}O_{2-\delta}$ (b) and Pr_6O_{11} (c) samples sintered at 1100 °C.

High oxygen mobility of Pr, Y- doped ceria and developed interface between disordered perovskite and fluorite domains in PNC – YDC composites provide high values of k_{chem} in the intermediate temperature range. This is in agreement with the EXAFS data, showing the important role of Pr incorporation into F phase in forming additional oxygen vacancies. These results are also in full agreement with the ones presented in our earlier studies [11] showing the presence of two channels of oxygen diffusion in PNC and PNC – YDC. The small amount of oxygen involved in fast diffusion channel can correspond to $PrO_{2-\delta}$ along

with surface defects (Fig. 12). Domination of the fast oxygen diffusion channel in PNC – YDC involving F domains and P+F interfaces was shown, so the oxygen transport in such nanocomposite is generally determined by F domains [14, 15, 35]. The results of CVR studies are also in agreement with TPD O_2 studies showing domination of intermediate-temperature desorption corresponding to removal of oxygen from F domains and P+F interfaces.

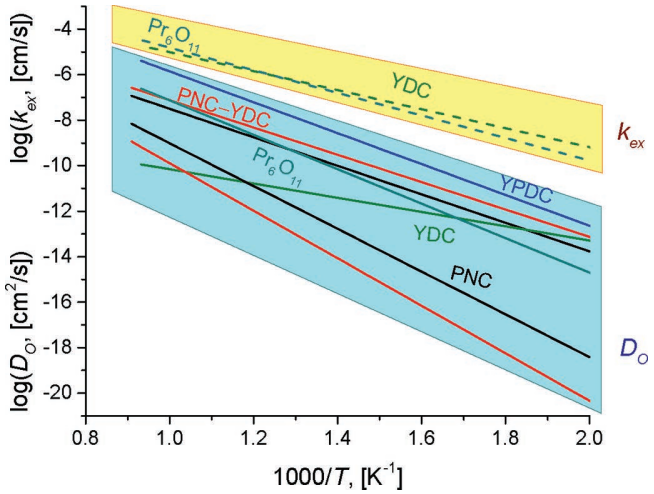

Fig. 12: Arrhenius plots for oxygen tracer diffusion coefficients (D_O) and surface exchange constant (k_{ex}) for various samples.

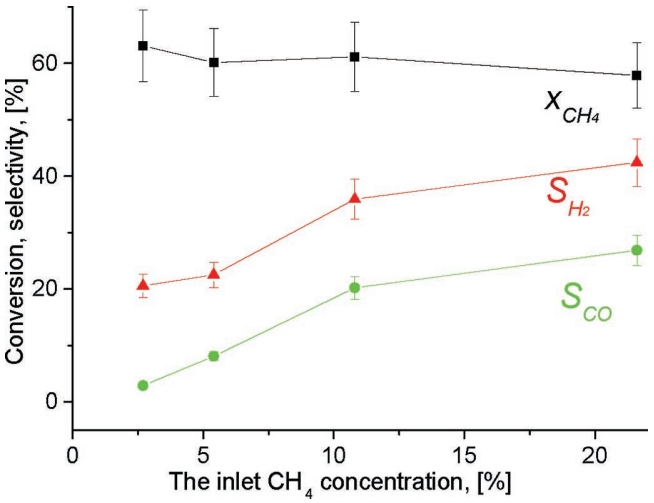

Fig. 13: The inlet CH_4 concentration effect on its conversion and selectivity at 950 °C for Pt/SPCZ | MF – GDC | PNC – YDC membrane. Flow rate is 2 l/h for gas mixture and air.

(3) Membrane testing

The performance of the membrane based on PNC – YDC nanocomposite deposited on Ni/Al foam substrate with MF – GDC buffer and Pt/SPCZ catalytic layers was studied. The oxygen flux under air/methane gradient is 2.5 ml $O_2 \cdot cm^{-2} \cdot min^{-1}$ for feed 21 % CH_4 and 10 ml $O_2 \cdot cm^{-2} min^{-1}$ for feed 50 – 100 % CH_4 at 950 °C. So, the oxygen permeability of the membrane meets criteria of the practical application [6]. Gas flow dynamics in double-flange assembly was studied earlier [39].

The selectivity of methane oxidation into syngas increases with the inlet methane concentration (Fig. 13), since the coverage of the catalytic particles' surface by reactive oxygen species decreases. Syngas yield and methane conversion increase with temperature and contact time, which is typical for such reactors. The outlet H_2 and CO concentrations ratio varies depending on contact time and the inlet carbon dioxide concentration (Fig. 14). H_2/CO concentration ratio is < 1 for contact times < 0.14 s at 950 °C and is > 1 at higher contact times (feed 46 % CO_2 + 48 % natural gas + N_2). CH_4 conversion is up to 60 %.

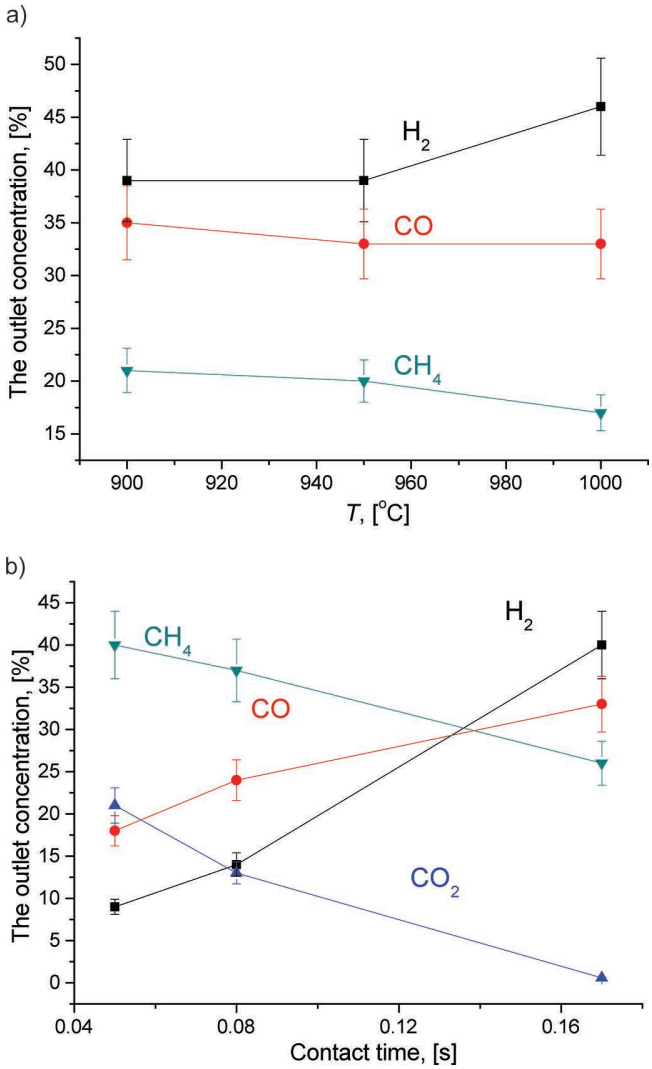

Fig. 14: Temperature (contact time 0.18 s) (a) and contact time (T = 950 °C) (b) effect on the outlet concentration of the natural gas oxi-dry reforming reagents and products for Ni/SmPrCeZrO | MF – GDC | PNC – YDC membrane. Feed 46 % CO_2 + 48 % natural gas + N_2.

Stable performance of the membrane was demonstrated for at least 200 h time-on-stream. Hence, the materials applied in this work are promising as functional components of membranes for the oxygen separation from air and methane oxidation into syngas by this oxygen.

As one can see from the concentrations vs temperature plots (Figs. 13 and 14b), the reaction temperature affects product yields dramatically. The unit used, double-flange assembly, allows us only to measure the housing temperature, but not the membrane's temperature, so a new measuring technique was developed for further investigation

of the membrane processes. Owing to the working range from 600 to 1000 °C, a membrane irradiates visible light, so an RGB image could be captured and further analyzed. A conventional NIR-pyrometry technique is not applicable here owing to the effect of water steam shading, since, as it is transparent to visible light, steam absorbs the membrane's IR radiation.

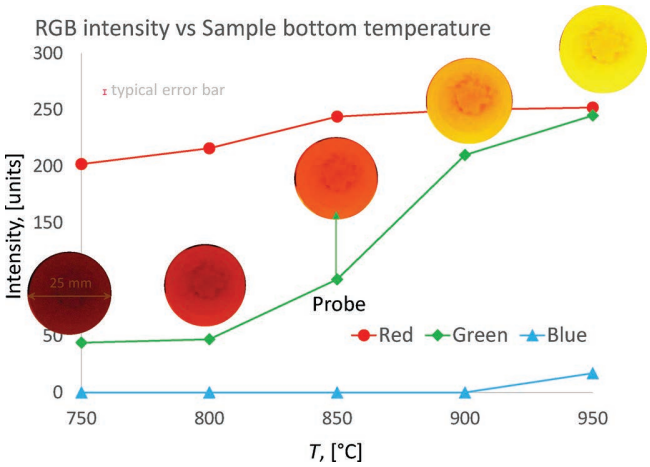

Fig. 15: Calibration curves for pyrometry.

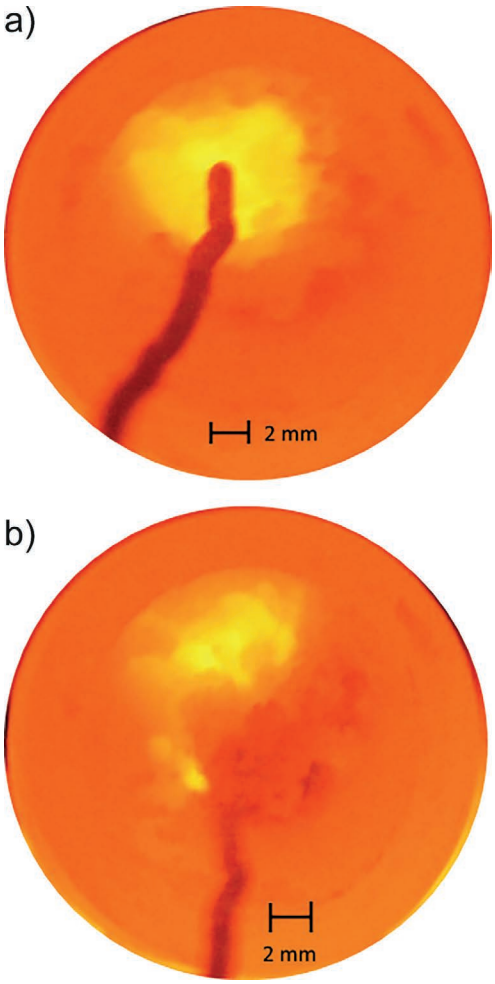

Fig. 16: The membrane test run footages in 20 % CH_4/80 % He + air at 845 °C.

Consisting of three colors with intensities from 0 to 256, each pixel gives temperature data, to obtain which one should make a calibration line or curve. Such a curve was obtained by shooting a membrane from 750 to 950 °C (Table 4 and Fig. 15). As it can be seen, the red line reaches its top at 850 °C, meanwhile the green line's intensity increases from 50 to 250 within the membrane working range, giving us less than one point for a degree as accuracy.

In this way the membrane temperature map could be obtained by shooting through the quartz window, and the very first footage shows the working conditions being far from isothermal (Fig. 16).

Table 4: RGB color of the pixel depending on temperature.

T, [°C]	RGB intensity, [units]		
	Red	Green	Blue
750	202	**44**	0
800	216	47	0
850	244	100	0
900	250	210	0
950	252	245	17

IV. Conclusions

Composites based on Ni-containing perovskite-like oxides and doped ceria demonstrate very high lattice oxygen mobility and surface reactivity owing to disordering caused by the redistribution of cations between phases. Detailed studies of the structure allowed to prove finally that namely regions of YDC domains enriched by Pr cations transferred from PNC domains on sintering are responsible for the emergence of a fast oxygen migration path in this system. High and stable performance was shown for long-time testing of the oxygen separation membrane with PNC – YDC-based functional layers.

Acknowledgements

Support was provided by the Russian Science Foundation (Project 16 – 13 – 00112). The work was done using the infrastructure of the Shared-Use Center "Siberian Synchrotron and Terahertz Radiation Center (SSTRC)" based on VEPP-3 of BINP SB RAS.

References

1 Sadykov, V., Mezentseva, N., Arapova, M., Krieger, T., Gerasimov, E., Alikina, G., Pelipenko, V., Bobin, A., Muzykantov, V., Fedorova, Y., Sadovskaya, E., Eremeev, N., Belyaev, V., Okhlupin, Y., Uvarov, N.: Fast oxygen transport in bismuth oxide containing nanocomposites, *Solid State Ionics*, **251**, 34 – 39, (2013).

2 Ji, Y., Kilner, J.A., Carolan, M.F.: Electrical properties and oxygen diffusion in yttria-stabilised zirconia (YSZ) – $La_{0.8}Sr_{0.2}MnO_{3\pm\delta}$ (LSM) composites, *Solid State Ionics*, **176**, 937 – 943, (2005).

3 Wincewicz, K.C., Cooper, J.S.: Taxonomies of SOFC material and manufacturing alternatives, *J. Power Sources*, **140**, 280 – 296, (2005).

4 Oh, D., Gostovic, D., Wachsman, E.D.: Mechanism of $La_{0.6}Sr_{0.4}Co_{0.2}Fe_{0.8}O_3$ cathode degradation, *J. Mater. Res.*, **27**, 1992 – 1999, (2012).

5 Bucher, E., Sitte, W.: Long-term stability of the oxygen exchange properties of $(La,Sr)_{1-z}(Co,Fe)O_{3-\delta}$ in dry and wet atmospheres, *Solid State Ionics*, **192**, 480 – 482, (2011).

6 Sadykov, V.A., Pavlova, S.N., Kharlamova, T.S., Muzykantov, V.S., Uvarov, N.F., Okhlupin, Y.S., Ishchenko, A.V., Bobin, A.S., Mezentseva, N.V., Alikina, G.M., Lukashevich, A.I., Krieger, T.A., Larina, T.V., Bulgakov, N.N., Tapilin, V.M., Belyaev, V.D., Sadovskaya, E.M., Boronin, A. I., Sobyanin, V.A., Bobrenok, O.F., Smirnova, A.L., Smorygo, O.L., Kilner, J.A.: Perovskites and their nanocomposites with fluorite-like oxides as materials for solid oxide fuel cells cathodes and oxygen-conducting membranes: Mobility and reactivity of the surface/bulk oxygen as a key factor of their performance. In: Perovskites: Structure, properties and uses. Nova Science Publishers, New York, USA, 2010.

7 Steele,B.C.H.: State-of-the-art SOFC ceramic materials. In: Proceedings of the 1. European SOFC Forum. Baden, Switzerland, 1994.

8 Sadykov, V., Smirnova, A., Lukashevich, A., Vostrikov, Z., Rogov, V., Krieger, T., Ishchenko, A., Zaikovsky, V., Bobrova, L., Ross, J., Smorygo, O., Smirnova, A., Rietveld, B., van Berkel, F.: Nanocomposite catalysts for steam reforming of methane and biofuels: Design and performance. In Advances in Nanocomposites - Synthesis, Characterization and Industrial Applications. InTech, Rijeka, Croatia, 2011.

9 Sadykov, V.A., Eremeev, N.F., Sadovskaya, E.M., Bobin, A.S., Fedorova, Y.E., Muzykantov, V.S., Mezentseva, N.V., Alikina, G.M., Kriger, T.A., Belyaev, V.D., Rogov, V.A., Ulikhin, A.S., Okhlupin, Y.S., Uvarov, N.F., Bobrenok, O.F., McDonald, N., Watton, J., Dhir, A., Steinberger-Wilckens, R., Mertens, J., Vinke, I.C.: Cathodic materials for intermediate-temperature solid oxide fuel cells based on praseodymium nickelates-cobaltites, *Russ. J. Electrochem.*, **50**, 669 – 679, (2014).

10 Sadykov, V., Eremeev, N., Alikina, G., Sadovskaya, E., Muzykantov, V., Pelipenko, V., Bobin, A., Krieger, T., Belyaev, V., Ivanov, V., Ishchenko, A., Rogov, V., Ulihin, A., Uvarov, N., Okhlupin, Y., Mertens, J., Vinke, I.: Oxygen mobility and surface reactivity of $PrNi_{1-x}Co_xO_{3+\delta} - Ce_{0.9}Y_{0.1}O_{2-\delta}$ cathode nanocomposites, *Solid State Ionics*, **262,** 707 – 712, (2014).

11 Sadykov, V., Eremeev, N., Sadovskaya, E., Bobin, A., Ishchenko, A., Pelipenko, V., Muzykantov, V., Krieger, T., Amanbaeva, D.: Oxygen mobility and surface reactivity of $PrNi_{1-x}Co_xO_{3-\delta}$ perovskites and their nanocomposites with $Ce_{0.9}Y_{0.1}O_{2-\delta}$ by temperature-programmed isotope exchange experiments, *Solid State Ionics*, **273**, 35 – 40, (2015).

12 Sadykov, V.A., Eremeev, N.F., Bolotov, V.A., Tanashev, Y.Y., Fedorova, Y.E., Amanbayeva, D.G., Bobin, A.S., Sadovskaya, E.M., Muzykantov, V.S., Pelipenko, V.V., Lukashevich, A.I., Krieger, T.A., Ishchenko, A.V., Smirnova, A.L.: The effect of microwave sintering on stability and oxygen mobility of praseodymium nickelates-cobaltites and their nanocomposites. *Solid State Ionics*, **288**, 76 – 81, (2016).

13 Sadykov, V.A., Pavlova, S.N., Vinokurov, Z.S., Shmakov, A.N., Eremeev, N.F., Fedorova, Y.E., Kriventsov, V.V., Bolotov, V.A., Tanashev, Y.Y., Sadovskaya, E.M., Cherepanova, S.V.: Application of SR methods for the study of nanocomposite materials for hydrogen energy, *Phys. Procedia*, **84,** 397 – 406 (2016).

14 Borchert, H., Frolova, Y.V., Kaichev, V.V., Prosvirin, I.P., Alikina, G.M., Lukashevich, A.I., Zaikovskii, V.I., Moroz, E.M., Trukhan, S.N., Ivanov, V.P., Paukshtis, E.A., Bukhtiyarov, V.I., Sadykov, V.A.: Electronic and chemical properties of nanostructured cerium dioxide doped with praseodymium, *J. Phys. Chem. B*, **109**, 5728 – 5738, (2005).

15 Sinev, M.Y., Graham, G.W., Haack, L.P., Shelef, M.: Kinetic and structural studies of oxygen availability of the mixed oxides $Pr_{1-x}M_xO_y$ (M = Ce, Zr), *J. Mater. Res.*, **11**, 1960 – 1971, (1996).

16 Tai, L.-W., Nasrallah, M.M., Anderson, H.U., Sparlin, D.M., Sehlin, S.R.: Structure and electrical properties of $La_{1-x}Sr_xCo_{1-y}Fe_yO_3$. Part 1. The system $La_{0.8}Sr_{0.2}Co_{1-y}Fe_yO_3$. *Solid State Ionics*, **76**, 259 – 271, (1995).

17 Sadykov, V.A., Pavlova, S., Zarubina, V., Bobin, A., Alikina, G., Lukashevich, A., Muzykantov, V., Usoltsev, V., Kharlamova, T., Boronin, A., Koscheev, S., Krieger, T., Ishchenko, A., Mezentseva, N., Salanov, A., Smirnova, A., Bobrenok, O., Uvarov, N.: Design and characterization of functionally graded cathode materials for solid oxide fuel cells. *ECS Trans.*, **25**, 2403 – 2412, (2009).

18 Sadykov, V., Mezentseva, N., Usoltsev, V., Sadovskaya, E., Ishchenko, A., Pavlova, S., Bespalko, Y., Kharlamova, T., Zevak, E., Salanov, A., Krieger, T., Belyaev, V., Bobrenok, O., Uvarov, N., Okhlupin, Y., Smorygo, O., Smirnova, A., Singh, P., Vlasov, A., Korobeynikov, M., Bryazgin, A., Kalinin, P., Arzhannikov, A.: Solid oxide fuel cell composite cathodes based on perovskite and fluorite structures, *J. Power Sources*, **196**, 7104 – 7109, (2011).

19 Sadykov, V., Alikina, G., Lukashevich, A., Muzykantov, V., Usoltsev, V., Boronin, A., Koscheev, S., Krieger, T., Ishchenko, A., Smirnova, A., Bobrenok, O., Uvarov, N.: Design and characterization of LSM/ScCeSZ nanocomposite as mixed ionic-electronic conducting material for functionally graded cathodes of solid oxide fuel cells. *Solid State Ionics*, **192**, 540 – 546, (2011).

20 Sadykov, V., Usoltsev, V., Yeremeev, N., Mezentseva, N., Pelipenko, V., Krieger, T., Belyaev, V., Sadovskaya, E., Muzykantov, V., Fedorova, Y., Lukashevich, A., Ishchenko, A., Salanov, A., Okhlupin, Y., Uvarov, N., Smorygo, O., Arzhannikov, A., Korobeynikov, M., Thumm, M.K.A.: Functional nanoceramics for intermediate temperature solid oxide fuel cells and oxygen separation membranes, *J. Eur. Ceram. Soc.*, **33**, 2241 – 2250, (2013).

21 Sadykov, V.A., Eremeev, N.F., Usol'tsev, V.V., Bobin, A.S., Alikina, G.M., Pelipenko, V.V., Sadovskaya, E.M., Muzykantov, V.S., Bulgakov, N.N., Uvarov, N.F.: Mechanism of oxygen transfer in layered lanthanide nickelates $Ln_{2-x}NiO_{4+\delta}$ (Ln = la, Pr) and their nanocomposites with $Ce_{0.9}Gd_{0.1}O_{2-\delta}$ and $Y_2(Ti_{0.8}Zr_{0.2})_{1.6}Mn_{0.4}O_{7-\delta}$ solid electrolytes, *Russ. J. Electrochem.*, **49**, 645 – 651, (2013).

22 Aulchenko, V.M., Evdokov, O.V., Kutovenko, V.D., Pirogov, B.Y., Sharafutdinov, M.R., Titov, V.M., Tolochko, B.P., Vasiljev, A.V., Zhogin, I. A., Zhulanov, V.V.: One-coordinate X-ray detector OD-3M. *Nucl. Instruments Methods Phys. Res. Sect. A Accel. Spectrometers, Detect. Assoc. Equip.*, **603**, 76 – 79, (2009).

23 Lutterotti, L., Wenk, H., Matthies, S.: MAUD (Material Analysis Using Diffraction): A user friendly Java program for Rietveld Texture Analysis and more. In: Proceeding of the Twelfth International Conference on Textures of Materials (ICOTOM-12). Montreal, Canada, 1999.

24 Loponov, K.N., Kriventsov, V.V., Nagabhushana, K.S., Boennemann, H., Kochubey, D.I., Savinova, E.R.: Combined *in situ* EXAFS and electrochemical investigation of the oxygen reduction reaction on unmodified and Se-modified Ru/C, *Catal. Today*, **147**, 260 – 269, (2009).

25 Koningsberger, D.C., Mojet, B.L., van Dorssen, G.E., Ramaker, D.E.: XAFS spectroscopy; fundamental principles and data analysis, *Top. Catal.*, **10**, 143 – 155, (2000).

26 Klementev, K.V.: Extraction of the fine structure from X-ray absorption spectra, *J. Phys. D. Appl. Phys.*, **34**, 209 – 217, (2001).

27 Sklyarov, A.V.: Reactions on catalyst surfaces under programmed-heating conditions, *Russ. Chem. Rev.*, **55**, 214 – 221, (1986).

28 Sadykov, V., Okhlupin, Y., Yeremeev, N., Vinokurov, Z., Shmakov, A., Belyaev, V., Uvarov, N., Mertens, J.: *In situ* X-ray diffraction studies of $Pr_{2-x}NiO_{4+\delta}$ crystal structure relaxation caused by oxygen loss, *Solid State Ionics*, **262**, 918 – 922, (2014).

[29] Huang, S., Lu, Q., Feng, S., Li, G., Wang, C.: $PrNi_{0.6}Co_{0.4}O_3 - Ce_{0.8}Sm_{0.2}O_{1.9}$ composite cathodes for intermediate temperature solid oxide fuel cells, *J. Power Sources*, **199**, 2012.

[30] Shannon, R.D.: Revised effective ionic radii and systematic studies of interatomic distances in halides and chalcogenides, *Acta Crystallogr. Sect. A*, **32**, 751 – 767, (1976).

[31] Takasu, Y., Sugino, T., Matsuda, Y.: Electrical conductivity of praseodymia doped ceria, *J. Appl. Electrochem.*, **14**, 79 – 81, (1984).

[32] Nauer, M., Ftikos, C., Steele, B.C.H.: An evaluation of Ce-Pr oxides and Ce-Pr-Nb oxides mixed conductors for cathodes of solid oxide fuel cells: structure, thermal expansion and electrical conductivity, *J. Eur. Ceram. Soc.*, **14**, 493 – 499, (1994).

[33] Ahn, K., Yoo, D.S., Prasad, D.H., Lee, H.-W., Chung, Y.-C., Lee, J.-H.: Role of multivalent pr in the formation and migration of oxygen vacancy in pr-doped Ceria: experimental and first-principles investigations, *Chem. Mater.*, **24**, 4261 – 4267, (2012).

[34] Sadykov, V.A., Kuznetsova, T.G., Alikina, G.M., Frolova, Y.V., Lukashevich, A.I., Muzykantov, V.S., Rogov, V.A., Batuev, L.C., Kriventsov, V.V., Kochubei, D.I., Moroz, E.M., Zyuzin, D.A., Paukshtis, E.A., Burgina, E.B., Trukhan, S.N., Ivanov, V.P., Pinaeva, L.G., Ivanova, Y.A., Kostrovskii, V.G., Neophytides, S., Kemnitz, E., Scheurel, K., Mirodatos, C.: Ceria-based fluorite-like oxide solid solutions promoted by precious metals as catalysts of methane transformation into syngas. In: New Topics in Catalysis Research. Nova Science Publishers, New York, 2007.

[35] Kim, J.J., Bishop, S.R., Thompson, N.J., Chen, D., Tuller, H.L.: Investigation of nonstoichiometry in oxide thin films by simultaneous *in situ* optical absorption and chemical capacitance measurements: Pr-doped ceria, a case study, *Chem. Mater.*, **26**, 1374 – 1379, (2014).

[36] Aksenova, T.V., Petrov, A.N., Cherepanov, V.A., Gavrilova, L.Y.: The thermodynamic parameters of oxygen nonstoichiometry defects in lanthanum cobaltite doped with acceptor impurities (Sr and Ni), *Russ. J. Phys. Chem.*, **80**, 1215 – 1220, (2006).

[37] Kiselev, E.A., Proskurnina, N.V., Cherepanov, V.A.: The oxygen nonstoichiometry, defect structure, and thermodynamic characteristics of disordering of nickel-and iron-substituted lanthanum cobaltites, *Russ. J. Phys. Chem. A*, **81**, 1950 – 1955, (2007).

[38] Islam, M.S.: Computer modelling of defects and transport in perovskite oxides, *Solid State Ionics*, **154**, 75 – 85, (2002).

[39] Shelepova, E., Vedyagin, A., Sadykov, V., Mezentseva, N., Fedorova, Y., Smorygo, O., Klenov, O., Mishakov, I.: Theoretical and experimental study of methane partial oxidation to syngas in catalytic membrane reactor with asymmetric oxygen-permeable membrane, *Catal. Today*, **268**, 103 – 110, (2016).